Hot Electron Preheat in Hydrodynamically Scaled Direct-Drive Inertial Confinement Fusion Implosions on the NIF and OMEGA

M. J. Rosenberg,[1, a)] A. A. Solodov,[1] C. Stoeckl,[1] M. Hohenberger,[2] R. Bahukutumbi,[1] W. Theobald,[1] D. Edgell,[1] T. Filkins,[1] R. Betti,[1] F. J. Marshall,[1] R. C. Shah,[1] D. P. Turnbull,[1] A. R. Christopherson,[2] N. Lemos,[2] E. Tubman,[2] and S. P. Regan[1]

[1)] *Laboratory for Laser Energetics, University of Rochester, Rochester, NY 14623, USA*

[2)] *Lawrence Livermore National Laboratory, Livermore, CA 94550, USA*

(Dated: 9 June 2023)

Hot electron preheat has been quantified in warm, directly-driven inertial confinement fusion implosions on OMEGA and the National Ignition Facility (NIF), to support hydrodynamic scaling studies. These CH-shell experiments were designed to be hydrodynamically equivalent, spanning a factor of 40 in laser energy and a factor of 3.4 in spatial and temporal scales, while preserving the incident laser intensity of 10^{15} W/cm^2. Experiments with similarly low levels of beam smoothing on OMEGA and NIF show a similar fraction ($\sim$0.2%) of laser energy deposited as hot electron preheat in the unablated shell on both OMEGA and NIF and similar preheat per mass ($\sim$2 kJ/mg), despite the NIF experiments generating a factor of three more hot electrons ($\sim$1.5% of laser energy) than on OMEGA ($\sim$0.5% of laser energy). This is plausibly explained by more absorption of hot electron energy in the ablated CH plasma on NIF due to larger areal density, as well as a smaller solid angle of the imploding shell as viewed from the hot electron generating region due to the hot electrons being produced at a larger standoff distance in lower-density regions by stimulated Raman scattering, in contrast to in higher-density regions by two-plasmon decay on OMEGA. The results indicate that for warm implosions at intensities of around 10^{15} W/cm^2, hydrodynamic equivalence is not violated by hot electron preheat, though for cryogenic implosions, the reduced attenuation of hot electrons in DT plasma will have to be considered.

I. INTRODUCTION

In direct-drive inertial confinement fusion (ICF),[1–3] laser light ablates a spherical shell in order to implode fusion fuel to temperatures and densities sufficient to initiate thermonuclear fusion reactions in the hot-spot region and ignite the capsule. Hot-spot ignition designs consist of cryogenic deuterium-tritium (DT) fuel inside of an ablator made of CH or other materials with high hydrodynamic efficiency. Currently, cryogenic direct-drive experiments are conducted at the 30-kJ OMEGA laser facility,[4] with the best-performing implosions having demonstrated an ignition threshold parameter[5] that, when scaled to the 2-MJ laser energy of the National Ignition Facility (NIF), is within 25% of ignition.[6] Direct-drive cryogenic implosions may be performed on NIF in the future. The factor of up to 70 extrapolation in laser energy and 4 in spatial dimension of cryogenic targets presents a challenge in projecting implosion performance from OMEGA to NIF. Though state-of-the-art radiation-hydrodynamics codes, benchmarked to experiments on OMEGA and NIF, are used to guide ignition designs, a simpler, hydrodynamic scaling[7] is presented as a first step or "baseline" for approximating expected direct-drive performance on NIF.

This scaling, based on analytic formulas predicated on a fixed implosion velocity, ablation pressure, and adiabat (the ratio of the pressure in the imploding shell to Fermi-degenerate pressure), describes how ICF observables should vary with laser energy or capsule dimensions, assuming that experiment inputs are appropriately scaled. Validity of, or deviation from, hydrodynamic scaling across the OMEGA/NIF energy scale can be assessed using experimental platforms available with current NIF capabilities and underpins the extrapolation to ignition scale. Hydrodynamic scaling in cylindrical implosions has been studied at OMEGA and NIF, showing similar levels of hydrodynamic instability growth, as expected.[8] The concept of hydrodynamic scaling has also been explored in simulations of direct-drive implosions.[7,9]

Deviation from hydrodynamic equivalence can be caused by various physical mechanisms whose relevant scale lengths do not increase linearly with spatial scale, such as electron thermal transport[7] or laser-plasma instabilities (LPI).[10] Hot electron preheat generated by LPI, which can degrade compressibility and implosion performance in cryogenic ICF implosions,[11] does not necessarily obey hydrodynamic scaling and must be measured empirically at the relevant scales. Previous experiments have studied hot electron preheat and its effects in planar[12–18] and spherical geometry[11,19–21] at a variety of intensities and scales[22] relevant to direct drive ICF, including approaching or achieving ignition-relevant scale legnths.

Here, hydrodynamically scaled OMEGA and NIF room temperature ("warm") target implosions, spanning a factor of 40 in laser energy and 3.4 in spatial and temporal scales and conducted in both symmetric direct drive (SDD) and polar direct drive (PDD)[23] illumina-

[a)] Electronic mail: mros@lle.rochester.edu

tion geometry, were used to study hot electron preheat at each scale to determine whether preheat causes deviation from hydrodynamic equivalence in warm implosions. While NIF preheat results were published previously,[20] this work significantly extends those findings to OMEGA scale, and incorporates x-ray imaging data at both scales, to assess the validity of hydrodynamic scaling. The results show that although more hot electrons are generated on NIF than on OMEGA, normalized to the incident laser energy, preheat energy deposited into the implosions scaled proportionally with laser energy. This result indicates that the validity of hydrodynamic scaling between OMEGA and NIF is not adversely affected by hot electron preheat in warm implosions.

This paper is organized as follows: principles of hydrodynamic scaling are outlined in Section II; experimental results from implosion experiments to evaluate hot electron preheat in hydro-scaled implosions on OMEGA and NIF are presented in Section III; interpretation of the data and its implications for extrapolating direct-drive implosion performance and hot electron preheat to ignition-relevant implosions, as well as future experiments, are discussed in Section IV; and concluding remarks are presented in Section V.

II. HYDRODYNAMIC SCALING

Hydrodynamic equivalence in direct-drive implosions[7] is predicated on the scale-invariance of the Euler equations describing conservation of mass, momentum, and energy. These equations can be written in dimensionless variables scaled by a single parameter that is equivalent to the Mach number. Implosions that are hydrodynamically equivalent are therefore defined by having the same Mach number and, consequently, the same implosion velocity, ablation pressure, and adiabat.[7] Time is proportional to linear spatial dimension. In order to maintain the same implosion velocity, the absorbed laser energy (assumed proportional to the incident laser energy) is proportional to the shell mass. Fixed ablation pressure requires that laser intensity be unchanged. This equivalence forces laser power to be proportional to the square of the capsule radius and, with time proportional to spatial dimension, laser energy to be proportional to the cube of the capsule radius, or volume. Mass density and energy density, and consequently pressure and temperature, are fixed.

These relationships determine the scaling of ICF observables for hydrodynamically equivalent implosions and can be used to assess the conformity with hydrodynamic scaling. For example, fusion yield, $Y \propto n^2\langle\sigma v\rangle V\tau$, where n is the reactant density, $\langle\sigma v\rangle$ is the fusion reactivity (strictly a function of temperature), V is the burn volume, and τ is the burn duration. With density and temperature fixed, the only scaled factors are the volume ($\propto R^3$ or E) and time ($\propto R$ or $E^{1/3}$). Therefore, yield scales like R^4 or $E^{4/3}$. A summary of ICF experimental inputs and their hydrodynamic scaling with spatial scale or laser energy is shown in Table I.

TABLE I. Idealized scaling of input experimental parameters for hydrodynamically equivalent implosions with either spatial dimension R or energy E.

Parameter	R Scaling	E Scaling
Time	$\propto R$	$\propto E^{1/3}$
Laser Intensity	Fixed	Fixed
Laser Power	$\propto R^2$	$\propto E^{2/3}$
Laser Energy	$\propto R^3$	$\propto E$
Shell Radius	$\propto R$	$\propto E^{1/3}$
Shell Thickness	$\propto R$	$\propto E^{1/3}$
Gas Density	Fixed	Fixed

Hydrodynamic scaling is intended as a simplified scaling that omits certain elements of physics not expected to be scale-invariant, such as LPI. Therefore, in order to evaluate the validity of hydrodynamic scaling in practice, it is essential to perform experiments that directly determine those effects at different scales.

III. HYDRODYNAMICALLY-SCALED HOT ELECTRON PREHEAT EXPERIMENTS

As hot electron preheat is a critical energy deposition mechanism that can hinder performance and affect extrapolation from OMEGA to NIF implosions, it is necessary to conduct experiments at each scale to determine the scaling of preheat under hydrodynamically equivalent conditions.

A. Implosion Design

D_2-gas-filled CH shell implosions have been studied extensively on NIF in the PDD configuration[23] to understand laser energy coupling, implosion symmetry, and cross-beam energy transfer mitigation at ignition-relevant scales.[24–26] These implosions, driven by 192 beams of 351 nm light divided into 48 sets of 4 beams ("quads"), were adapted for studies of hot electron preheat. The capsules consisted of glow-discharge polymer (GDP) CH shells, some of which contained a Ge dopant at nominally ∼4% atomic concentration over an inner layer of the shell in order to diagnose hot electron energy deposition.[11,20] The principle of the experiment is that for nominally identical implosions, with the same target diameter, shell mass, and laser intensity, the implosions containing the Ge dopant will produce more hard x rays due to the higher atomic number, with the difference in hard x-ray energy between experiments with and without the dopant, or with different thicknesses of the Ge-doped layer, being used to infer the hot electron energy deposited in the various layers.

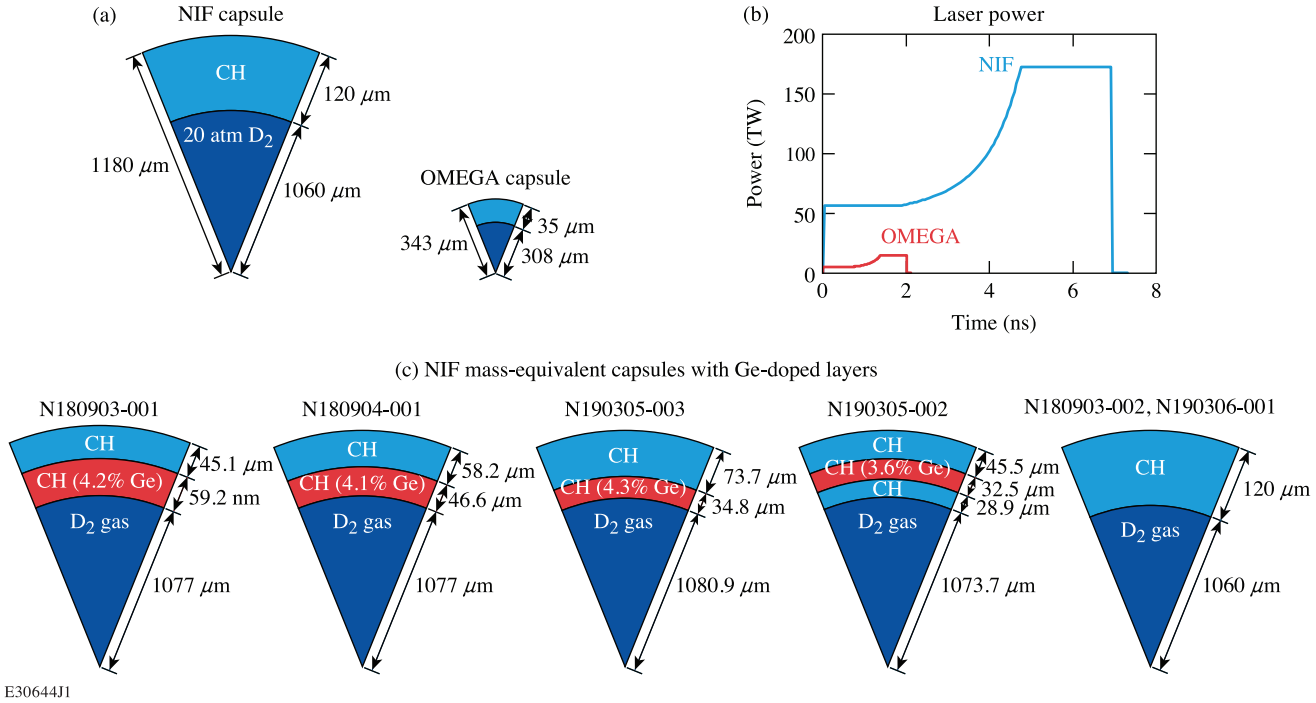

FIG. 1. (Color online) Nominal (a) capsule dimensions and (b) laser pulses used in hydrodynamically-scaled NIF and OMEGA direct drive implosion experiments with pure CH ablators. Thickness and placement of Ge-doped layers in NIF implosions is shown in (c). The NIF portion of the figure is partially reprinted with permission from A. A. Solodov *et al.*, Phys. Rev. E, **106**, 055204 (2022), Ref. [20]. Copyright 2022 by the American Physical Society.

The nominal thickness for pure CH shells was 120 μm, with the thickness for shells containing Ge adjusted in a way that preserved mass equivalence. The nominal shell diameter was 2360 μm, with 20 atm of D_2 gas. The 6.9-ns laser pulse design was similar to those used in previous NIF PDD implosions,[24,25] with a 2-ns foot, followed by an exponential ramp to a 2-ns flat top. The foot power was doubled to 56.8 TW to increase the adiabat (from 2.8 to 3.8 according to simulations) and provide better implosion stability. Peak power was nominally 173 TW, with a total laser energy of 732 kJ. The incident laser intensity was 10^{15} W/cm^2. Ge-dopant layer thicknesses were either 59.2 μm, 46.6 μm, 34.8 μm over the inner portion of the shell, or 32.5 μm at a depth of 28.9 μm from the inner shell surface. These NIF experiments were previously reported in Ref. [20].

Following the relationships in Table I, scaled implosions were designed at a laser energy of 18 kJ on OMEGA, limited by the available energy to illuminate the target in PDD using 40 beams. The incident laser intensity was designed to match that on NIF. The shells were nominally 686 μm in diameter, with a pure-CH thickness of 35 μm and the same 20-atm D_2 fill. On OMEGA, inner 4.3% to 4.4% Ge-doped layer thicknesses of 10.6 μm or 16.5 μm were used in some experiments, mass equivalent to the pure-CH shells and close to hydro-equivalent to two of the NIF capsule designs with Ge dopant. The laser pulse was 2.0 ns in duration, with a peak power of 14.6 TW. Capsules were illuminated in both symmetric direct drive (SDD, 60 beams) and polar drive (40 beams) configurations. Nominal capsule and laser properties for the NIF and OMEGA experiments are illustrated in Figure 1(a)-(b), while the thickness and position of Ge-doped layers in NIF implosions is illustrated in Fig. 1(c).

Though the implosions were designed to be hydrodynamically equivalent, differences in OMEGA and NIF laser drive may be expected to affect adherence to hydrodynamic scaling as well as hot electron preheat. In addition to the one-dimensional (1D) laser energy coupling and energy transport considerations mentioned in Section II, multi-dimensional effects due to laser-beam smoothing seeding hydrodynamic instabilities and the polar drive configuration may affect the implosion. On NIF, laser smoothing consisted of 1D smoothing by spectral dispersion (SSD)[27] at a bandwidth of 90 GHz. For this study, implosions on OMEGA were conducted either with 2D SSD with a bandwidth of 0.3 THz,[28] or with no SSD modulation. OMEGA experiments used polarization wedges[29] for additional smoothing and, as such, the no-SSD experiments are considered to have laser smoothing approximately equivalent to NIF. On OMEGA, the SDD experiments were conducted either with or without SSD, while the PDD experiments were only conducted without SSD. The NIF PDD laser beam pointing consisted of 4 rings at different polar angles in each hemisphere,[20,24] while OMEGA PDD[30] uses 3 ringsat port angles of 21°, 42°, and 59°, pointed to 112 μm, 143

μm, or 196 μm above or below the target center along the symmetry axis, with a defocus of 0.06, 0.1, or 0.18 mm, respectively. The beam spot sizes and shapes as determined by distributed phase plates (DPP)[31] also do not exactly scale between OMEGA and NIF. No wavelength detuning was used on either facility.

B. Simulations

Radiation-hydrodynamics simulations using the 1D code LILAC[32] illustrate the degree to which hydrodynamic scaling is expected to be followed in these NIF and OMEGA implosions. The simulations included nonlocal electron thermal transport,[33] first principles equation of state tables,[34] and multi-group diffusion radiation transport. Laser energy deposition was modeled using three-dimensional laser ray trace with cross-beam energy transfer.[35] Laser beam profiles were approximated by a super-Gaussian of 4.5 order with $1/e$ radius of 860 μm on the NIF and fits of measured profiles on OMEGA (close to super-Gaussian of 4.2 order with $1/e$ radius of 286 μm, as determined by the DPP).[36] Figure 2 shows the radial shell positions (outer, inner, and maximum-density) and the shell velocities as functions of time in the simulations for the nominal hydro-scaled plastic-shell targets on (a) the NIF and (b) OMEGA. Fig. 2 demonstrates that the implosions are almost hydro-equivalent with nearly the same shell velocities and shell positions close to hydro-equivalent as both NIF and OMEGA implosions converge by about a factor of 1.75 in the middle of the flat-top porton of the laser pulse. Although these simulations do not capture the multi-dimensional effects of the PDD implosions, they indicate a good hydro-equivalence in the NIF and OMEGA experiments overall.

C. Experimental Results

Data were obtained on six NIF experiments, two with pure CH ablators and four with Ge-doped layers of various thicknesses. For OMEGA, ten experiments were conducted, three with pure CH ablators and seven with Ge-doped layers. Of the OMEGA experiments, three were in symmetric drive with SSD, three were in symmetric drive without SSD, and four were in polar drive without SSD. Average as-shot laser and capsule parameters are summarized in Table II. The experimental conditions closely follow the hydrodynamic scaling prescription, especially for the PDD implosions without SSD.

Time-gated x-ray self-emission images, from which implosion trajectory and shape are inferred, demonstrate that hydrodynamic scaling was approximately satisfied across the OMEGA and NIF experiments to within measurement uncertainty. Images and inferred ablation-front trajectories are shown in Figure 3. NIF images were obtained using hardened gated x-ray detectors (HGXD),[37] examples of which from shot N180903-002 are shown in

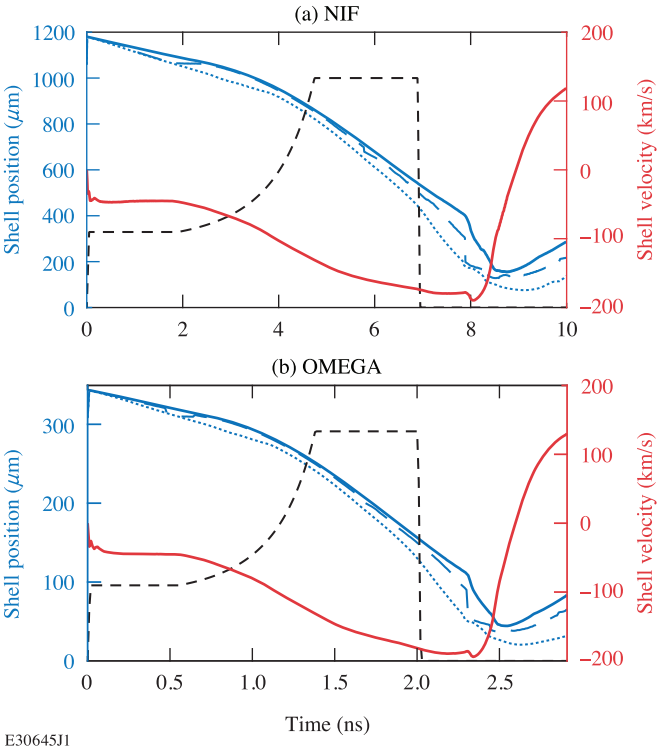

FIG. 2. (Color online) 1D LILAC-simulated outer $1/e$ of maximum (blue solid), inner $1/e$ of maximum (blue dotted), and maxium-density (blue dashed) shell position, shell velocity (red) and laser pulse shape (black dashed) as a function of time for nominally hydrodynamically-equivalent CH-shell direct drive implosions on (a) NIF and (b) OMEGA. The time and spatial axes are hydrodynamically scaled. The calculations predict implosion properties close to hydro-equivalent.

Figure 3(a). The images show the emergence of even-mode (Legendre polynomials of mode 2, 4, and 6) asymmetries as the shell convergences by a factor of ~2 until $t = 7$ ns, shortly after the laser turns off. The shell is slightly oblate as a consequence of the polar drive geometry with DPPs optimized for indirect drive. X-ray framing camera images were obtained on OMEGA at a polar angle of 100.81°, slightly below the equator. Example images from an OMEGA PDD implosion, shot 96840, are shown in Figure 3(b). The images show a qualitatively similar shell morphology to those on NIF despite differences in the polar drive illumination, though the mode 4 asymmetry is less pronounced on OMEGA. The qualitative similarity of the gated x-ray images are sufficient to demonstrate that implosion morphology does not significantly affect the comparison of 1D energetics and preheat scaling.

The ablation front radius for both NIF and OMEGA implosions is taken to be the angular average radius of the surface of steepest gradient of x-ray emission, as in previous studies of laser energy coupling in NIF and OMEGA direct-drive implosions.[26,38,39] Three sets of implosion trajectory data from each of NIF and OMEGA are shown to demonstrate shot-to-shot repeatability and the equiv-

TABLE II. Average experiment parameters on NIF, scaled value based on 18 kJ laser energy, and actual parameters on OMEGA. The uncertainties represent standard deviations over the ensemble of 6 NIF shots and 10 OMEGA shots. OMEGA experiments are categorized by either symmetric direct drive (SDD) or polar direct drive (PDD), and by SSD being on or off. Capsule thickness is averaged over two CH-only experiments on NIF, and a single CH-only experiment in each category on OMEGA

Parameter	NIF	Scaled to 18 kJ	OMEGA SDD SSD on	OMEGA SDD SSD off	OMEGA PDD SSD off
Laser energy (kJ)	715±6	18	19.2±0.1	18.9±0.4	17.7±0.05
Peak laser power (TW)	172±2	14.8	16.2±0.2	16.9±0.4	15.1±0.1
Capsule diameter (μm)	2366±7	693	684±3	687±4	684±6
Capsule thickness (μm)	118.2±0.1	34.6	34.4	34.1	34.4

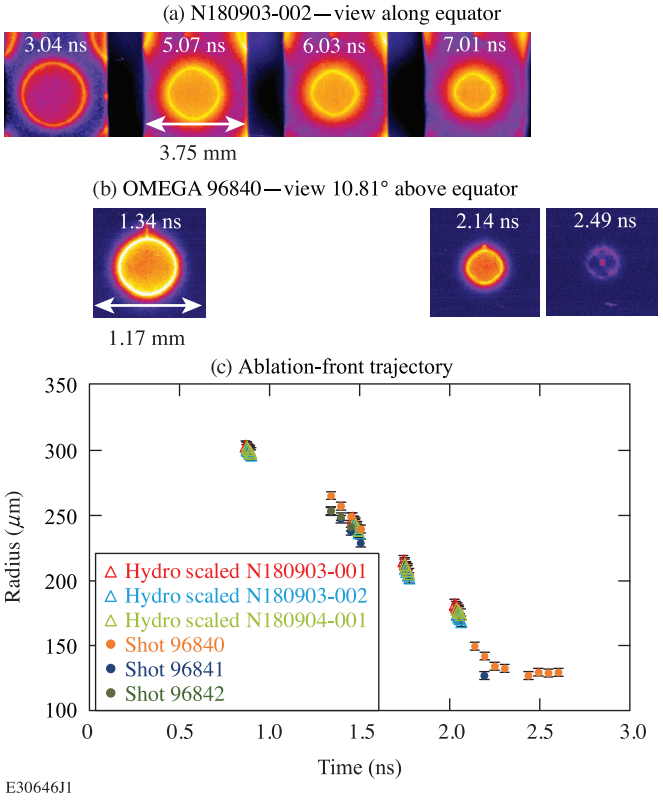

FIG. 3. (Color online) X-ray self-emission data from PDD implosions, including (a) images obtained on the NIF equator on shot N180903-002, (b) images obtained at an angle of 10.81° off of the equator on OMEGA shot 96840 and (c) inferred ablation-front radii as a function of time, with NIF data points hydrodynamically scaled to 18 kJ energy.

alence of implosions with and without Ge dopant. The ablation front trajectories from OMEGA implosions are shown, overlaid with the hydrodynamically-scaled NIF ablation front trajectories, in Figure 3(c). The shells have converged to a similar radius at the OMEGA-equivalent time of $t = 1.5$ ns. For OMEGA trajectories, a nominal uncertainty of ± 3 μm is used, based on the ratio of image noise to the x-ray emission gradient length around the ablation front,[38] inferred from a sample image on shot 96840 around $t = 1.5$ ns. This error bar is also approximately the standard deviation in the inferred radius from 72 lineouts at different azimuthal angles around the image. For NIF, the standard deviation in the inferred steepest-gradient radius around the image is 14 μm which, scaled to OMEGA dimensions, corresponds to a nominal uncertainty of ± 4 μm. The absolute timing on OMEGA is accurate to approximately ± 50 ps, while the inter-strip timing is known to roughly ± 20 ps.

The implosion velocity on OMEGA appears slightly faster than that on NIF between $t = 1.5$ and $t = 2.1$ ns, with an average velocity of 118±6 μm/ns on NIF, while OMEGA shot 96840 has a velocity of 144±8 μm/ns. This may be due in part to subtle deviation from hydrodynamic equivalence in the experimental input conditions or reduced energy coupling due to greater cross-beam energy transfer (CBET) on NIF. LILAC simulations show a reduction in energy coupling during peak power due to CBET by 32% on NIF and by 27% on OMEGA. Overall the energetics are approximately comparable throughout the pulse. That the convergence ratio of the shell at the end of the pulse is similar suggests that the comparison of inferred hot electron preheat deposited in the unablated shell for NIF and OMEGA implosions is valid.

Importantly, scattered light data demonstrate that, for both NIF and OMEGA implosions, the presence of the Ge dopant does not affect the laser-plasma interactions and therefore the hot electron source. Figure 4 shows time-resolved scattered light data, either the average of SRS-band fast diode measurements obtained in full aperture backscatter stations (FABS) covering eight beam ports at 30° and 50° from the south pole on NIF[40] [Fig. 4(a)] or the FABS-measured half-harmonic ($\omega/2$) emission from the time-resolved optical streak camera in Beam 25 on OMEGA [Fig. 4(b)].[41] As demonstrated previously, the NIF scattered light spectrum consists entirely of SRS features,[13,24] while OMEGA implosions generated $\omega/2$ light indicative of TPD.[42] The NIF experiments shown here are shots N180903-001, N180903-002, N180904-001 [see Fig. 1(c)]. The OMEGA experiments are four PDD shots with SSD off, one with a pure CH ablator, two with a 10.6 μm Ge-doped CH layer, and one with a 16.5 μm Ge-doped CH layer. The NIF time axis is absolute, while the OMEGA time axis is arbitrary, with the curves shifted so that their falling edges line up,

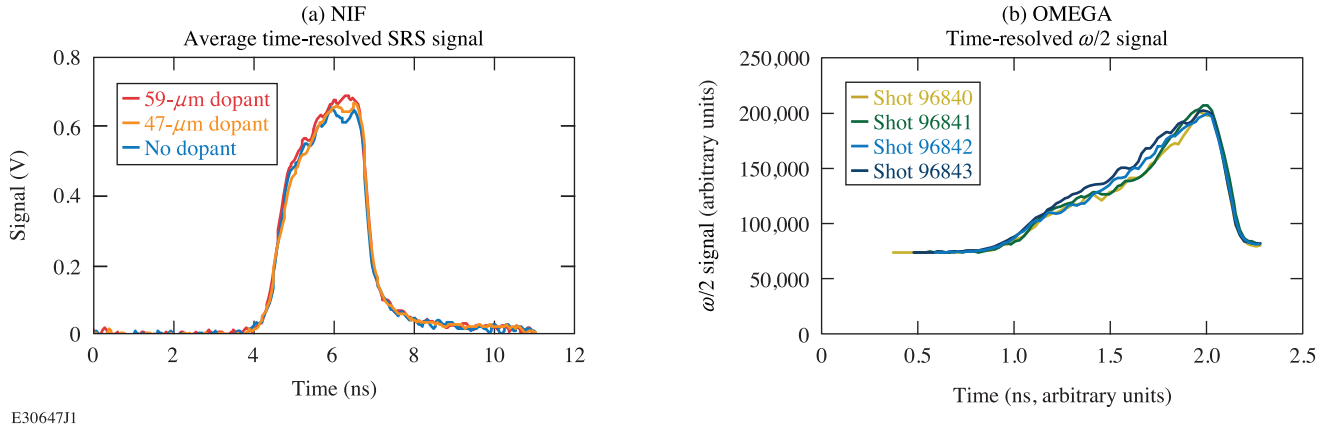

FIG. 4. (Color online) Time-resolved scattered light data obtained in FABS from (a) NIF implosions, for experiments with varying thicknesses of the Ge-doped layer (including none) and (b) OMEGA PDD implosions without SSD. The NIF data are SRS scattered light averaged over eight FABS beams, while he OMEGA data are $\omega/2$ emission from TPD obtained in a single FABS. The NIF data are absolutely timed, while the OMEGA data have been shifted on the arbitrary time axis to line up the peak of the signal. Both sets of experiments show that scattered light, and therefore the underlying hot-electron generation processes, are not affected by Ge in the unablated shell (OMEGA shots 96840, 96842, and 96843 contained Ge dopant).

expected to correspond to the end of the laser pulse. In both cases, the curves for scattered light on implosions at each facility overlay almost exactly. The NIF SRS signal is fairly constant with time throughout the period corresponding to peak power, while the OMEGA $\omega/2$ signal increases nearly linearly with time, with a peak at the end of the laser pulse. Both data sets confirm that, at each scale, LPI and hot electron production were identical in experiments with or without Ge dopant.

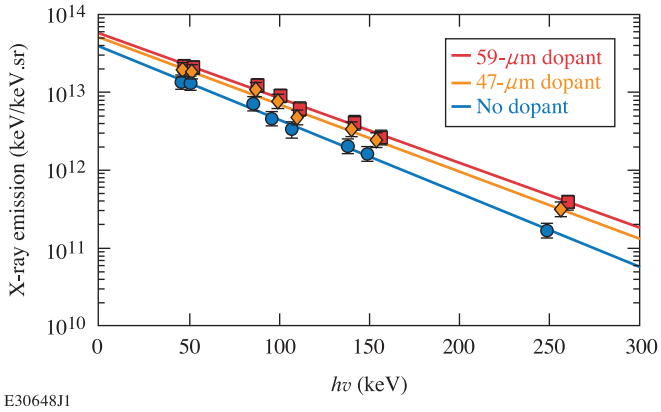

FIG. 5. (Color online) Time-integrated hard x-ray spectra inferred from eight channels of FFLEX data on NIF, for experiments with varying thicknesses of the Ge-doped layer, corresponding to the same experiments for which SRS data is shown in Figure 4(b). Though a simple thick-target bremsstrahlung (exponential) fit is shown here, the data were analyzed using a Monte Carlo model of hot electron transport (see Fig. 1(h) in Ref. [20]).

Hot electron preheat was inferred from hard x-ray measurements obtained using the filter fluorescer x-ray (FFLEX) diagnostic on NIF[43] and the hard x-ray detector (HXRD) on OMEGA.[44,45] The FFLEX signal with up to 10 channels is fit using a Monte Carlo model of hot electron energy deposition and resulting hard x-ray emission.[14,20] Hard x-ray spectra inferred from FFLEX measurements in three experiments with different amounts of Ge dopant, corresponding to the scattered light data in Figure 4(b), are shown in Figure 5. The single-temperature fits to the 8 channels shows similar hard x-ray slope temperatures ($T_{\rm hot}$ = 56±2 keV) and total hard x-ray emission that increases with the amount of Ge dopant, as expected.[11,20] Analysis of the NIF data was presented in Ref. [20]. The OMEGA HXRD consists of scintillators filtered to be sensitive to x rays above energies of ∼40 keV, ∼60 keV, and ∼80 keV. The signal is fit to a single-temperature (1-T) hot electron model ($T_{\rm hot}$ = 50±5 keV) based on the preheat formula as described in Ref. [11]. Each diagnostic is absolutely calibrated, so that the absolute hard x-ray fluence is measured, allowing for inference of absolute hot electron energy deposited. The difference in time-integrated hard x-ray fluence between experiments with Ge-doped layers with different thicknesses was related to the profile of hot electron energy deposition using either Geant4 Monte Carlo modeling for NIF data[20] or a formula[11] for preheat in different layers for OMEGA data.

The hard x-ray spectrum fit using 8 FFLEX channels on the NIF, spanning the energy range from 50 to 250 keV, ensures a good accuracy of the measured hard x-ray energy and slope temperature. 3D Maxwellian electron distributions were used in the analysis of the NIF and OMEGA experiments, for which the hot-electron temperature coincides with the slope temperature of the bremsstrahlung emission in a thick target,[46,47] which has been confirmed by Geant4 Monte Carlo simulations. Hard x-ray measurements using HXRD have been recently compared to the measurements using other two hard x-ray detectors[48] available on OMEGA: the hard x-

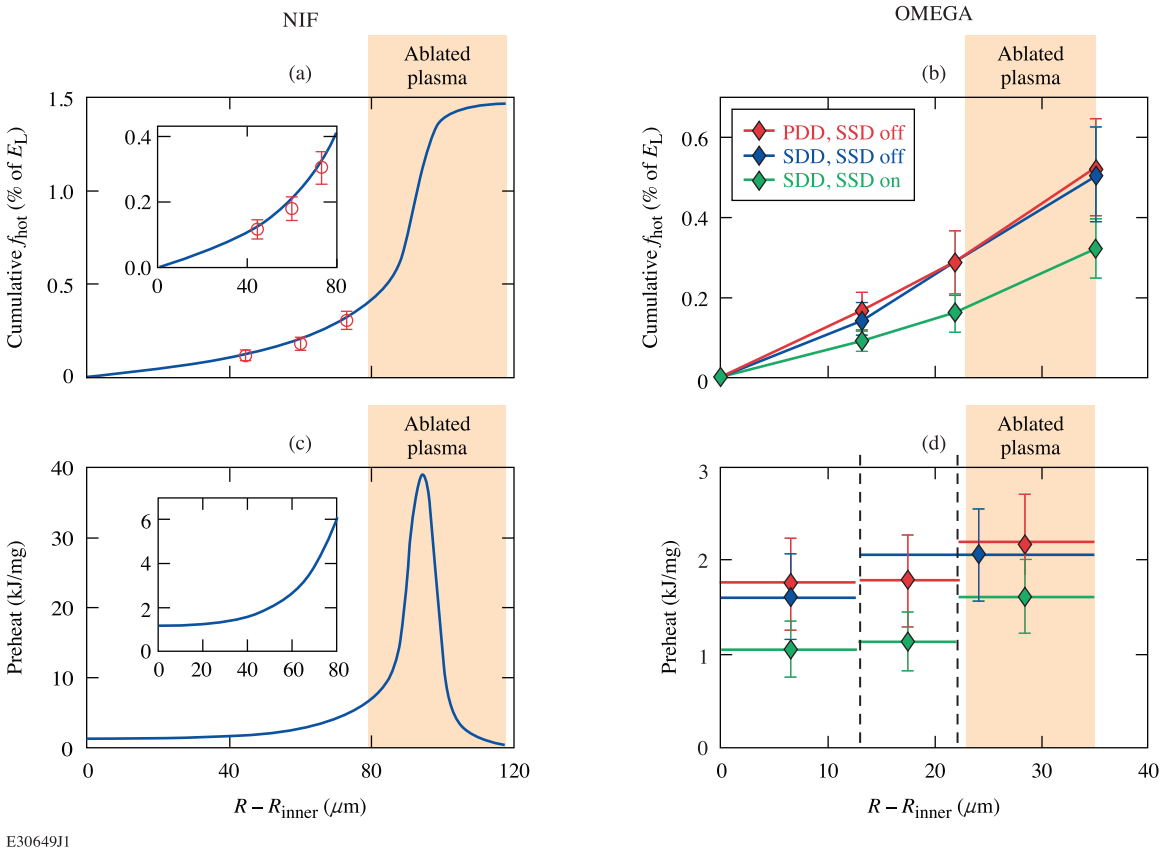

FIG. 6. (Color online) Inferred cumulative hot electron fraction (f_{hot}) as a function of position in the shell (R_{inner} representing the inner shell surface) for (a) NIF and (b) OMEGA experiments. The local deposited preheat per mass, proportional to the radial derivative of the curves in (a)-(b), are shown for NIF and OMEGA in (c) and (d) respectively. The NIF curves are a Monte Carlo model fit to the experimental data points, while the OMEGA data are obtained using the preheat formula from Ref. [11]. OMEGA data were obtained for symmetric direct drive (SDD) either with (green) or without (blue) SSD, and for polar direct drive (PDD) without SSD (red). OMEGA SDD experiments with SSD off used only one thickness of the Ge-doped layer so the average preheat per mass is averaged over a larger region. NIF data [(a),(c)] were originally published in Ref. [20] and are reprinted with permission from A. A. Solodov *et al.*, Phys. Rev. E, **106**, 055204 (2022). Copyright 2022 by the American Physical Society.

ray image plate (HXIP) and the bremsstrahlung MeV x-ray spectrometer (BMXS). HXIP and BMXS have been used to diagnose hot-electron production in several other experiments, particularly in the laser-plasma interaction experiments at shock-ignition relevant laser intensities,[15,16,22] some of which utilized K-shell emission from fluorescent Cu tracer layers to complement the hard x-ray measurements. Although some disagreement in x-ray slope temperature using these three detectors was observed[48] due to uncertainties in the instrument response functions, the disagreement was small (<10 keV) around 50 keV, the temperature in the present experiment. This uncertainty is not expected to significantly affect the validity of these results.

Potential uncertainty from Monte Carlo simulations, which are widely used to study the transport of hot electrons in the experiments but do not account for ionization effects and possible electromagnetic fields in a plasma, are likewise not expected to significantly alter the present findings. It has been specified that a target in the plasma state stops and diffuses electrons more effectively than a cold target,[49] although this is expected to have a weak or limited effect in the dense plastic shell (undoped or doped with Ge), where the temperature is within 15 to 30 eV according to hydrodynamic simulations in our experiments and the plasma is weakly ionized. As suggested by Geant4 simulations, the dominant contribution to the bremsstrahlung emission comes from the energetic electrons depositing most of their energy in the dense shell. Resistive electric fields were found to slow down fast electrons[50–52] in solid-target experiments at the laser intensities exceeding 10^{18} W/cm^2, relevant to fast ignition, however, this effect was found to be negligible[50,52] for the laser intensities below (2 to 5)x10^{15} W/cm^2, relevant to direct drive. Hot-electron bremsstrahlung emission is not affected by the target ionization, except for the low-energy photons below ~5 to 10 keV (irrelevant to our analysis), for which the details of nuclei screening

by atomic or plasma electrons become important in the emission process.[53]

The preheat formula uses the stopping power valid for a plasma[54] and has been extensively tested and found to be accurate for implosions on OMEGA, where the preheat per fuel mass is approximately uniform.[11,55]. Detailed Monte Carlo simulations, however, are appropriate for the NIF experiments, where hot-electron energy deposition in the shell is very nonuniform.

The inferred cumulative hot electron fraction ($f_{\rm hot} = E_{\rm hot}/E_{\rm laser}$) as a function of position within the initial shell and the local deposition of hot electron energy per mass are shown for NIF and OMEGA hydrodynamically scaled implosions in Figure 6. The NIF experiments show a total $f_{\rm hot}$ of 1.5% [Figure 6(a)], most of which is absorbed in the ablated plasma, consisting of the outer 40 μm of initial shell material. The local deposited preheat energy, which is effectively proportional to the radial derivative of the cumulative $f_{\rm hot}$, is likewise highest in the ablated plasma region [Figure 6(c)]. Within the unablated, imploding shell, about 0.4% of laser energy is deposited as preheat, which rapidly falls to around 0.2% over the inner ∼80% of shell material while the local preheat energy per mass is around 1.5 kJ/mg at the innermost shell region. On OMEGA, the total hot electron fraction is lower, around 0.5% for PDD or SDD implosions with SSD off (around 0.3% for SDD implosions with SSD on), though the preheat energy deposited in the unablated shell is similar to NIF. On OMEGA, with SSD off, around 0.3% of laser energy is deposited as hot electron preheat into the entirety of the unablated shell, and around 0.15% into the inner 60% of unablated shell. With SSD on, preheat is reduced by approximately 40%. The primary difference between preheat profiles on NIF and OMEGA implosions is the absorption of hot electron energy in the ablated plasma, which is significantly lower on OMEGA. On OMEGA with SSD off, the average preheat per mass over the outer unablated shell and ablated plasma is only ∼2 kJ/mg, falling slightly to around 1.6 kJ/mg in the innermost shell, which is comparable to the preheat per mass in the inner portion of the shell on NIF [Figure 6(c)-(d)].

IV. DISCUSSION

The profiles of deposited hot electron preheat on OMEGA and NIF support several takeaways. Most saliently, the results demonstrate the validity of hydrodynamic scaling, at least with respect to hot electron preheat, of warm CH implosions. The fraction of laser energy deposited into the shell and the local deposition of preheat energy per mass are within ∼10% of each other on OMEGA and NIF. Therefore, the impact of preheat on implosion behavior is inferred to be similar on OMEGA and NIF and does not affect hydrodynamic scaling, despite differences in the underlying LPI behavior (i.e. TPD on OMEGA versus SRS on NIF). For example, the expectation that areal density scales with the scale factor is not expected to be violated by preheat.

One important observation from the difference in total hot electron production on OMEGA and NIF, despite similar levels of preheat deposited in the shell, is that absorption of hot electron energy in the ablated plasma is a significant effect. This difference in hot electron attenuation in the ablated plasma between NIF and OMEGA may plausibly be attributed to two factors. One is the hot electron source, which on NIF is SRS[13,56,57] and on OMEGA is TPD.[42] Because TPD occurs at higher densities than SRS (0.25 $n_{\rm c}$ for TPD versus 0.15 to 0.25 $n_{\rm c}$ for SRS[57]) hot electrons are produced at a smaller radius on OMEGA and therefore the unablated shell effectively has a larger solid angle as viewed from the hot electron-producing region and intercepts a higher fraction of hot electrons. The other, more straightforward factor, is the areal density of the ablated plasma, which is expected to be larger on NIF by a factor of ∼3.4 based on the longer scale length and therefore to absorb more hot electron energy.

Within the OMEGA results, it is inferred that laser illumination geometry (PDD or SDD) does not strongly affect preheat. Though there is a caveat that the PDD experiments had ∼10% lower laser energy and power, the local deposited preheat energy and the cumulative hot electron fraction are not significantly different. In addition, the SSD beam smoothing on OMEGA reduces preheat by ∼40%.

These results also contribute to an extrapolation of hot electron preheat in ignition-scale cryogenic PDD implosions on NIF, which was presented briefly in Ref. [20] and is expanded upon here. This extrapolation starts with the NIF warm implosion results that showed ∼0.2% of laser energy coupled as preheat into the inner 80% of unablated shell at an intensity of 10^{15} W/cm^2.

Firstly, the density scale length is expected to be ∼30-50% larger in ignition designs[58] than in the NIF warm implosions, with a capsule diameter of ∼3 mm. Planar experiments with CH slab targets at scale lengths comparable to ignition-scale implosions[14] produced up to $f_{\rm hot}$ = 2%, ∼30% higher than the 1.5% observed in the warm implosions studied herein. Additionally, the extrapolation in hot electron production from OMEGA to subscale NIF implosions, from 0.5% to 1.5%, accompanied a three-fold increase in scale length. Therefore, since hot electron production increased a factor of three for a three-fold increase in scale length from OMEGA to NIF, another 40% increase in scale length may be expected to increase hot electron production by ∼40%. This extrapolation is also similar to the estimate based on the difference between NIF planar and spherical experiments. Therefore, it is expected that the increased scale length will generate ∼40% more hot electrons.

On the other hand, the increased convergence ratio in ignition designs will result in less hot electron energy being deposited in the unablated shell due to the reduced solid angle as viewed from the hot electron producing

region. The trajectory data shown above confirm that in these warm implosions, the shell converged by no more than a factor of two during the laser pulse, when hot electrons were generated. However, ignition designs are expected to converge by a factor of ∼2-3 during the pulse, conferring a reduction of shell solid angle by a factor of ∼2. Therefore, the hot electron energy coupled to the shell in ignition designs will be only half of that in the warm implosions studied here. This can be controlled by changing the laser pulse to alter the convergence during peak power.

An additional effect is the absorption of hot electron energy in the ablated plasma. In contrast to the warm, CH ablators studied here, cryogenic target direct drive implosions will partially ablate the DT ice layer. The DT plasma will less effectively shield the unablated shell from hot electrons. Monte Carlo calculations indicate that that profile of preheat deposited in the unablated imploding shell will be more radially uniform with DT than with CH. The local deposited preheat energy per mass at the outer edge of unablated shell is calculated to be ∼20% lower with DT than CH, though the local preheat at the inner shell/vapor interface is calculated to increase by >50%. Overall, the total amount of preheat in the inner 80% of unablated shell is not expected to be significantly changed with DT instead of CH.

Therefore, combining all of the factors above, an ignition-scale cryogenic implosion at the same intensity as the warm experiments discussed here may be expected to have similar or slightly higher hot electron preheat, around 0.1 to 0.2% of laser energy in the inner 80% of unablated DT. This is close to levels predicted to be tolerable in direct-drive ignition designs,[59] though this limit depends strongly on design parameters such as the implosion adiabat. Preheat may be mitigated by use of Si layers, which has been found to reduce preheat by a factor of 2 in both planar[14] and spherical[20] experiments on NIF, or by mid-Z dopants in the ablator. Enhanced beam smoothing, if implemented on NIF, may also reduce preheat, as it has been shown to do so in these OMEGA experiments by 40%. Laser intensity also affects the level of preheat, and future experiments will determine the intensity scaling of preheat at ignition-relevant scale lengths on NIF. Upcoming experiments will also directly assess the scaling of hot electron preheat on NIF between the 2.3 mm (730 kJ laser energy) and 3 mm (1.5 MJ) scales. These results can also be applied to calculate the expected effect of hot electron preheat in integrated simulations of ICF implosions.[11,21]

V. CONCLUSIONS

In summary, hot electron preheat has been measured in hydrodynamically-equivalent direct drive implosions on NIF and OMEGA. Polar-direct drive implosions with a similar, limited degree of beam smoothing at an intensity of 10^{15} W/cm^2 show around 0.2% of laser energy coupled to the inner portion of unablated shell in experiments both on NIF at target diameters and laser energies of 2.4 mm and 730 kJ and at 0.69 mm and 18 kJ on OMEGA. Measured implosion trajectories confirm the expected hydrodynamic scaling. These results indicate that hot electron preheat does not invalidate hydrodynamic scaling of warm implosions between OMEGA and NIF scales at ignition-relevant intensities for the implosion designs currently studied. OMEGA experiments show little variation in preheat as a function of symmetric or polar beam geometry, and a 40% reduction when 2-D smoothing by spectral dispersion is applied. Overall hot electron generation is a factor of 3 higher on NIF despite similar deposited preheat due to attenuation of hot electrons in the long-scale-length ablated plasma. Extrapolation of plasma conditions to ignition-relevant cryogenic implosions at NIF scale suggests that preheat will be at a tolerable level for intensities around and below 10^{15} W/cm^2.

ACKNOWLEDGMENTS

The authors thank NIF and OMEGA operations and target fabrication for their assistance in executing these experiments. This material is based upon work supported by the Department of Energy National Nuclear Security Administration under Award Number DE-NA0003856, the University of Rochester, and the New York State Energy Research and Development Authority.

This report was prepared as an account of work sponsored by an agency of the U.S. Government. Neither the U.S. Government nor any agency thereof, nor any of their employees, makes any warranty, express or implied, or assumes any legal liability or responsibility for the accuracy, completeness, or usefulness of any information, apparatus, product, or process disclosed, or represents that its use would not infringe privately owned rights. Reference herein to any specific commercial product, process, or service by trade name, trademark, manufacturer, or otherwise does not necessarily constitute or imply its endorsement, recommendation, or favoring by the U.S. Government or any agency thereof. The views and opinions of authors expressed herein do not necessarily state or reflect those of the U.S. Government or any agency thereof.

AUTHOR DECLARATIONS

Conflict of Interest

The authors have no conflicts to disclose.

Author Contributions

To be added.

DATA AVAILABILITY

The data that support the findings of this study are available from the corresponding author upon reasonable request.

[1] S. Atzeni and J. Meyer-Ter-Vehn, *The Physics of Inertial Fusion: Beam Plasma Interaction, Hydrodynamics, Hot Dense Matter*, International Series of Monographs on Physics (Clarendon, Oxford, 2004).

[2] R. S. Craxton, K. S. Anderson, T. R. Boehly, V. N. Goncharov, D. R. Harding, J. P. Knauer, R. L. McCrory, P. W. McKenty, D. D. Meyerhofer, J. F. Myatt, *et al.*, Physics of Plasmas **22**, 110501 (2015).

[3] E. Campbell, V. Goncharov, T. Sangster, S. Regan, P. Radha, R. Betti, J. Myatt, D. Froula, M. Rosenberg, I. Igumenshchev, *et al.*, Matter and Radiation at Extremes **2**, 37 (2017).

[4] T. R. Boehly, D. L. Brown, R. S. Craxton, R. L. Keck, J. P. Knauer, J. H. Kelly, T. J. Kessler, S. A. Kumpan, S. J. Loucks, S. A. Letzring, *et al.*, Opt. Commun. **133**, 495 (1997).

[5] R. Betti, A. R. Christopherson, B. K. Spears, R. Nora, A. Bose, J. Howard, K. M. Woo, M. J. Edwards, and J. Sanz, Phys. Rev. Lett. **114**, 255003 (2015).

[6] A. Lees, R. Betti, J. Knauer, V. Gopalaswamy, D. Patel, K. Woo, K. Anderson, E. Campbell, D. Cao, J. Carroll-Nellenback, *et al.*, Physics of Plasmas **30**, 012709 (2023).

[7] R. Nora, R. Betti, K. S. Anderson, A. Shvydky, A. Bose, K. M. Woo, A. R. Christopherson, J. A. Marozas, T. J. B. Collins, P. B. Radha, S. X. Hu, R. Epstein, F. J. Marshall, R. L. McCrory, T. C. Sangster, and D. D. Meyerhofer, Physics of Plasmas **21**, 056316 (2014), https://doi.org/10.1063/1.4875331.

[8] S. Palaniyappan, J. P. Sauppe, B. J. Tobias, C. F. Kawaguchi, K. A. Flippo, A. B. Zylstra, O. L. Landen, D. Shvarts, E. Malka, S. H. Batha, P. A. Bradley, E. N. Loomis, N. N. Vazirani, L. Kot, D. W. Schmidt, T. H. Day, R. Gonzales, and J. L. Kline, Physics of Plasmas **27**, 042708 (2020), https://doi.org/10.1063/1.5144608.

[9] A. Bose, K. M. Woo, R. Betti, E. M. Campbell, D. Mangino, A. R. Christopherson, R. L. McCrory, R. Nora, S. P. Regan, V. N. Goncharov, T. C. Sangster, C. J. Forrest, J. Frenje, M. Gatu Johnson, V. Y. Glebov, J. P. Knauer, F. J. Marshall, C. Stoeckl, and W. Theobald, Phys. Rev. E **94**, 011201 (2016).

[10] W. L. Kruer, *The physics of laser plasma interactions* (Addison-Wesley, Redwood City, CA, 1988).

[11] A. Christopherson, R. Betti, C. Forrest, J. Howard, W. Theobald, J. Delettrez, M. Rosenberg, A. Solodov, C. Stoeckl, D. Patel, *et al.*, Physical Review Letters **127**, 055001 (2021).

[12] B. Yaakobi, P.-Y. Chang, A. Solodov, C. Stoeckl, D. Edgell, R. Craxton, S. Hu, J. Myatt, F. Marshall, W. Seka, *et al.*, Physics of Plasmas (1994-present) **19**, 012704 (2012).

[13] M. J. Rosenberg, A. A. Solodov, J. F. Myatt, W. Seka, P. Michel, M. Hohenberger, R. W. Short, R. Epstein, S. P. Regan, E. M. Campbell, T. Chapman, C. Goyon, J. E. Ralph, M. A. Barrios, J. D. Moody, and J. W. Bates, Phys. Rev. Lett. **120**, 055001 (2018).

[14] A. A. Solodov, M. J. Rosenberg, W. Seka, J. F. Myatt, M. Hohenberger, R. Epstein, C. Stoeckl, R. W. Short, S. P. Regan, P. Michel, T. Chapman, R. K. Follett, J. P. Palastro, D. H. Froula, P. B. Radha, J. D. Moody, and V. N. Goncharov, Physics of Plasmas **27**, 052706 (2020), https://doi.org/10.1063/1.5134044.

[15] S. Zhang, C. M. Krauland, J. Peebles, J. Li, F. N. Beg, N. Alexander, W. Theobald, R. Betti, D. Haberberger, E. M. Campbell, R. Yan, E. Borwick, C. Ren, and M. S. Wei, Physics of Plasmas **27** (2020), 10.1063/1.5119250, 023111, https://pubs.aip.org/aip/pop/article-pdf/doi/10.1063/1.5119250/15775021/023111_1_online.pdf.

[16] A. Tentori, A. Colaitis, W. Theobald, A. Casner, D. Raffestin, A. Ruocco, J. Trela, E. Le Bel, K. Anderson, M. Wei, B. Henderson, J. Peebles, R. Scott, S. Baton, S. A. Pikuz, R. Betti, M. Khan, N. Woolsey, S. Zhang, and D. Batani, Physics of Plasmas **28** (2021), 10.1063/5.0059651, 103302, https://pubs.aip.org/aip/pop/article-pdf/doi/10.1063/5.0059651/15882865/103302_1_online.pdf.

[17] L. Antonelli, J. Trela, F. Barbato, G. Boutoux, P. Nicolaï, D. Batani, V. Tikhonchuk, D. Mancelli, A. Tentori, S. Atzeni, A. Schiavi, F. Baffigi, G. Cristoforetti, S. Viciani, L. A. Gizzi, M. Smid, O. Renner, J. Dostal, R. Dudzak, L. Juha, and M. Krus, Physics of Plasmas **26** (2019), 10.1063/1.5119697, 112708, https://pubs.aip.org/aip/pop/article-pdf/doi/10.1063/1.5119697/12608102/112708_1_online.pdf.

[18] G. Cristoforetti, P. Koester, S. Atzeni, D. Batani, S. Fujioka, Y. Hironaka, S. Hüller, T. Idesaka, K. Katagiri, K. Kawasaki, and et al., High Power Laser Science and Engineering **11**, e24 (2023).

[19] B. Yaakobi, A. A. Solodov, J. F. Myatt, J. A. Delettrez, C. Stoeckl, and D. H. Froula, Physics of Plasmas **20**, 092706 (2013), http://dx.doi.org/10.1063/1.4824008.

[20] A. Solodov, M. Rosenberg, M. Stoeckl, A. Christopherson, R. Betti, P. Radha, C. Stoeckl, M. Hohenberger, B. Bachmann, R. Epstein, *et al.*, Physical Review E **106**, 055204 (2022).

[21] D. Barlow, T. Goffrey, K. Bennett, R. H. H. Scott, K. Glize, W. Theobald, K. Anderson, A. A. Solodov, M. J. Rosenberg, M. Hohenberger, N. C. Woolsey, P. Bradford, M. Khan, and T. D. Arber, Physics of Plasmas **29** (2022), 10.1063/5.0097080, 082704, https://pubs.aip.org/aip/pop/article-pdf/doi/10.1063/5.0097080/16778467/082704_1_online.pdf.

[22] R. H. H. Scott, K. Glize, L. Antonelli, M. Khan, W. Theobald, M. Wei, R. Betti, C. Stoeckl, A. G. Seaton, T. D. Arber, D. Barlow, T. Goffrey, K. Bennett, W. Garbett, S. Atzeni, A. Casner, D. Batani, C. Li, and N. Woolsey, Phys. Rev. Lett. **127**, 065001 (2021).

[23] S. Skupsky, J. A. Marozas, R. S. Craxton, R. Betti, T. J. B. Collins, J. A. Delettrez, V. N. Goncharov, P. W. McKenty, P. B. Radha, T. R. Boehly, J. P. Knauer, F. J. Marshall, D. R. Harding, J. D. Kilkenny, D. D. Meyerhofer, T. C. Sangster, and R. L. McCrory, Physics of Plasmas **11**, 2763 (2004).

[24] M. Hohenberger, P. B. Radha, J. F. Myatt, S. LePape, J. A. Marozas, F. J. Marshall, D. T. Michel, S. P. Regan, W. Seka, A. Shvydky, *et al.*, Physics of Plasmas **22**, 056308 (2015), http://aip.scitation.org/doi/pdf/10.1063/1.4920958.

[25] P. B. Radha, M. Hohenberger, D. H. Edgell, J. A. Marozas, F. J. Marshall, D. T. Michel, M. J. Rosenberg, W. Seka, A. Shvydky, T. R. Boehly, T. J. B. Collins, E. M. Campbell, R. S. Craxton, J. A. Delettrez, S. N. Dixit, J. A. Frenje, D. H. Froula, V. N. Goncharov, S. X. Hu, J. P. Knauer, R. L. McCrory, P. W. McKenty, D. D. Meyerhofer, J. Moody, J. F. Myatt, R. D. Petrasso, S. P. Regan, T. C. Sangster, H. Sio, S. Skupsky, and A. Zylstra, Physics of Plasmas **23**, 056305 (2016), https://doi.org/10.1063/1.4946023.

[26] J. A. Marozas, M. Hohenberger, M. J. Rosenberg, D. Turnbull, T. J. B. Collins, P. B. Radha, P. W. McKenty, J. D. Zuegel, F. J. Marshall, S. P. Regan, T. C. Sangster, W. Seka, E. M. Campbell, V. N. Goncharov, M. W. Bowers, J.-M. G. Di Nicola, G. Erbert, B. J. MacGowan, L. J. Pelz, and S. T. Yang, Phys. Rev. Lett. **120**, 085001 (2018).

[27] S. Skupsky, R. W. Short, T. Kessler, R. S. Craxton, S. Letzring, and J. M. Soures, Journal of Applied Physics **66**, 3456 (1989), http://dx.doi.org/10.1063/1.344101.

[28] S. P. Regan, J. A. Marozas, J. H. Kelly, T. R. Boehly, W. R. Donaldson, P. A. Jaanimagi, R. L. Keck, T. J. Kessler, D. D. Meyerhofer, W. Seka, S. Skupsky, and V. A. Smalyuk, J. Opt. Soc. Am. B **17**, 1483 (2000).

[29]T. R. Boehly, V. A. Smalyuk, D. D. Meyerhofer, J. P. Knauer, D. K. Bradley, R. S. Craxton, M. J. Guardalben, S. Skupsky, and T. J. Kessler, Journal of Applied Physics **85**, 3444 (1999), https://doi.org/10.1063/1.369702.

[30]F. J. Marshall, P. B. Radha, M. J. Bonino, J. A. Delettrez, R. Epstein, V. Y. Glebov, D. R. Harding, C. Stoeckl, J. A. Frenje, M. Gatu Johnson, F. H. Séguin, H. Sio, A. Zylstra, and E. Giraldez, Physics of Plasmas **23** (2016), 10.1063/1.4940939, 012711, https://pubs.aip.org/aip/pop/article-pdf/doi/10.1063/1.4940939/15715301/012711_1_online.pdf.

[31]T. J. Kessler, Y. Lin, J. J. Armstrong, and B. Velazquez, in *Laser Coherence Control: Technology and Applications*, Vol. 1870 (SPIE, 1993) pp. 95–104.

[32]J. Delettrez, R. Epstein, M. C. Richardson, P. A. Jaanimagi, and B. L. Henke, Phys. Rev. A **36**, 3926 (1987).

[33]V. Goncharov, T. Sangster, P. Radha, R. Betti, T. Boehly, T. Collins, R. Craxton, J. Delettrez, R. Epstein, V. Y. Glebov, *et al.*, Physics of Plasmas **15**, 056310 (2008).

[34]S. Hu, L. Collins, V. Goncharov, J. Kress, R. McCrory, S. Skupsky, *et al.*, Physical Review E **92**, 043104 (2015).

[35]I. V. Igumenshchev, D. H. Edgell, V. N. Goncharov, J. A. Delettrez, A. V. Maximov, J. F. Myatt, W. Seka, A. Shvydky, S. Skupsky, and C. Stoeckl, Physics of Plasmas **17**, 122708 (2010), http://dx.doi.org/10.1063/1.3532817.

[36]W. Theobald, D. Cao, R. C. Shah, C. A. Thomas, I. V. Igumenshchev, K. A. Bauer, R. Betti, M. J. Bonino, E. M. Campbell, A. R. Christopherson, K. Churnetski, D. H. Edgell, C. J. Forrest, J. A. Frenje, M. Gatu Johnson, V. Y. Glebov, V. N. Goncharov, V. Gopalaswamy, D. R. Harding, S. X. Hu, S. T. Ivancic, D. W. Jacobs-Perkins, R. T. Janezic, T. Joshi, J. P. Knauer, A. Lees, R. W. Luo, O. M. Mannion, F. J. Marshall, Z. L. Mohamed, S. F. B. Morse, D. Patel, J. L. Peebles, R. D. Petrasso, P. B. Radha, H. G. Rinderknecht, M. J. Rosenberg, S. Sampat, T. C. Sangster, W. T. Shmayda, C. M. Shuldberg, A. Shvydky, C. Sorce, C. Stoeckl, M. D. Wittman, and S. P. Regan, Physics of Plasmas **29**, 012705 (2022), https://doi.org/10.1063/5.0072579.

[37]S. Glenn, J. Koch, D. K. Bradley, N. Izumi, P. Bell, G. Stone, R. Prasad, A. MacKinnon, P. Springer, O. L. Landen, and G. Kyrala, Rev. Sci. Inst. **81**, 10E539 (2010).

[38]D. Michel, A. Davis, W. Armstrong, R. Bahr, R. Epstein, V. Goncharov, M. Hohenberger, I. Igumenshchev, R. Jungquist, D. Meyerhofer, and et al., High Power Laser Science and Engineering **3**, e19 (2015).

[39]A. K. Davis, D. T. Michel, R. S. Craxton, R. Epstein, M. Hohenberger, T. Mo, and D. H. Froula, Review of Scientific Instruments **87**, 11E340 (2016), https://aip.scitation.org/doi/pdf/10.1063/1.4962191.

[40]J. D. Moody, P. Datte, K. Krauter, E. Bond, P. A. Michel, S. H. Glenzer, L. Divol, C. Niemann, L. Suter, N. Meezan, *et al.*, Review of Scientific Instruments **81**, 10 (2010).

[41]W. Seka, H. A. Baldis, J. Fuchs, S. P. Regan, D. D. Meyerhofer, C. Stoeckl, B. Yaakobi, R. S. Craxton, and R. W. Short, Phys. Rev. Lett. **89**, 175002 (2002).

[42]W. Seka, D. H. Edgell, J. F. Myatt, A. V. Maximov, R. W. Short, V. N. Goncharov, and H. A. Baldis, Physics of Plasmas **16**, 052701 (2009), http://dx.doi.org/10.1063/1.3125242.

[43]M. Hohenberger, F. Albert, N. E. Palmer, J. J. Lee, T. Döppner, L. Divol, E. L. Dewald, B. Bachmann, A. G. MacPhee, G. LaCaille, *et al.*, Review of Scientific Instruments **85**, 11 (2014).

[44]C. Stoeckl, V. Y. Glebov, D. D. Meyerhofer, W. Seka, B. Yaakobi, R. P. J. Town, and J. D. Zuegel, Review of Scientific Instruments **72**, 1197 (2001), https://doi.org/10.1063/1.1322621.

[45]D. Michel, A. Maximov, R. Short, J. Delettrez, D. Edgell, S. Hu, I. Igumenshchev, J. Myatt, A. Solodov, C. Stoeckl, *et al.*, Physics of Plasmas (1994-present) **20**, 055703 (2013).

[46]K. A. Brueckner, Phys. Rev. Lett. **36**, 677 (1976).

[47]R. P. Drake, R. E. Turner, B. F. Lasinski, E. A. Williams, K. Estabrook, W. L. Kruer, E. M. Campbell, and T. W. Johnston, Phys. Rev. A **40**, 3219 (1989).

[48]M. Stoeckl and A. Solodov, Nuclear Instruments and Methods in Physics Research Section A: Accelerators, Spectrometers, Detectors and Associated Equipment **931**, 162 (2019).

[49]A. Tentori, A. Colaïtis, and D. Batani, Matter and Radiation at Extremes **7** (2022), 10.1063/5.0103632, 065903, https://pubs.aip.org/aip/mre/article-pdf/doi/10.1063/5.0103632/16562724/065903_1_online.pdf.

[50]A. R. Bell, J. R. Davies, S. Guerin, and H. Ruhl, Plasma Physics and Controlled Fusion **39**, 653 (1997).

[51]J. R. Davies, Phys. Rev. E **65**, 026407 (2002).

[52]L. Volpe, D. Batani, A. Morace, and J. J. Santos, Physics of Plasmas **20** (2013), 10.1063/1.4771586, 013104, https://pubs.aip.org/aip/pop/article-pdf/doi/10.1063/1.4771586/13429720/013104_1_online.pdf.

[53]J. D. Jackson, in *Classical Electrodynamics, 2nd ed.* (John Wiley and Sons, New York, 1975) p. 717.

[54]A. A. Solodov and R. Betti, Physics of Plasmas **15** (2008), 10.1063/1.2903890, 042707, https://pubs.aip.org/aip/pop/article-pdf/doi/10.1063/1.2903890/13598330/042707_1_online.pdf.

[55]A. Christopherson, R. Betti, C. Forrest, J. Howard, W. Theobald, E. Campbell, J. Delettrez, M. Rosenberg, A. Solodov, C. Stoeckl, *et al.*, Physics of Plasmas **29**, 122703 (2022).

[56]P. Michel, M. J. Rosenberg, W. Seka, A. A. Solodov, R. W. Short, T. Chapman, C. Goyon, N. Lemos, M. Hohenberger, J. D. Moody, S. P. Regan, and J. F. Myatt, Phys. Rev. E **99**, 033203 (2019).

[57]M. J. Rosenberg, A. A. Solodov, W. Seka, R. K. Follett, J. F. Myatt, A. V. Maximov, C. Ren, S. Cao, P. Michel, M. Hohenberger, J. P. Palastro, C. Goyon, T. Chapman, J. E. Ralph, J. D. Moody, R. H. H. Scott, K. Glize, and S. P. Regan, Physics of Plasmas **27**, 042705 (2020), https://doi.org/10.1063/1.5139226.

[58]T. J. B. Collins and J. A. Marozas, Physics of Plasmas **25**, 072706 (2018), https://doi.org/10.1063/1.5039513.

[59]J. A. Delettrez, T. J. B. Collins, and C. Ye, Physics of Plasmas **26**, 062705 (2019), https://doi.org/10.1063/1.5089890.